Inorganic Chemistry
Article
pubs.acs.org/IC

Rapid Synthesis and Efficient Electrocatalytic Oxygen Reduction/Evolution Reaction of $CoMn_2O_4$ Nanodots Supported on Graphene

Jing Du,[†] Chengcheng Chen,[†] Fangyi Cheng,[†] and Jun Chen*[,†,‡]

[†]Key Laboratory of Advanced Energy Materials Chemistry (Ministry of Education) and [‡]Collaborative Innovation Center of Chemical Science and Engineering (Tianjin), Nankai University, Tianjin 300071, China

S Supporting Information

ABSTRACT: Transition-metal oxides have attracted extensive interest as oxygen-reduction/evolution reaction (ORR/OER) catalyst alternatives to precious Pt-based materials but generally exhibit limited electrocatalytic performance due to their large overpotential and low specific activity. We here report a rapid synthesis of spinel-type $CoMn_2O_4$ nanodots (NDs, below 3 nm) monodispersed on graphene for highly efficient electrocatalytic ORR/OER in 0.1 M KOH solution. The preparation of the composite involves the reaction of manganese and cobalt salts in mixed surfactant−solvent−water solution at mild temperature (120 °C) and air. $CoMn_2O_4$ NDs homogeneously distributed on carbonaceous substrates show strong coupling and facile charge transfer. Remarkably, graphene-supported $CoMn_2O_4$ NDs showed 20 mV higher ORR half-wave potential, twice the kinetic current, and better catalytic durability compared to the benchmark carbon-supported Pt nanoparticles (Pt/C). Moreover, $CoMn_2O_4$/reduced graphene oxide afforded electrocatalytic OER with a current density of 10 mA cm^{-2} at a low potential of 1.54 V and a small Tafel slope of ~56 mV/dec. This indicates that the composite of $CoMn_2O_4$ nanodots monodispersed on graphene is promising as highly efficient bifunctional electrocatalysts of ORR and OER that can be used in the areas of fuel cells and rechargeable metal−air batteries.

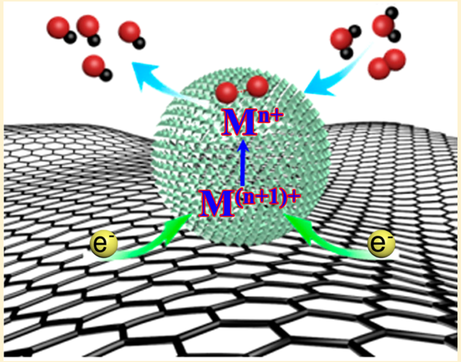

INTRODUCTION

The electrocatalytic oxygen reduction reaction (ORR) is of paramount importance in electrochemical energy storage and conversion technologies such as fuel cells and metal−air batteries.[1−6] Although Pt-based materials have shown the best performance for ORR, the cost and scarcity limit their widespread application.[7−10] Tremendous interest has been directed to earth-abundant 3d metal (Mn, Fe, Co, Ni) oxides.[11−21] Among these oxides, spinel oxides have attracted particular interest because of their high ORR activity, excellent stability, and low cost. The general formula of spinel oxide is AB_2O_4, in which A is in a tetrahedral site and B is in an octahedral site. We have reported that $Co_xMn_{3-x}O_4$ spinel nanoparticles prepared under ambient conditions were used as electrocatalysts for ORR/oxygen evolution reaction (OER).[22] However, neat $Co_xMn_{3-x}O_4$ affords inferior activity due to poor electrical conductivity. This means that the use of a conducting additive such as carbon is necessary. Recent studies have indicated that metal−oxide nanoparticles supported on graphene result in significantly enhanced catalytic activities due to oxide−carbon interaction.[13,23,24] As an example, Dai and co-workers have prepared cubic spinel phase $MnCo_2O_4$ (~5 nm) supported on N-doped reduced graphene by a solvothermal method at 150 °C, showing that the hybrids exhibited high ORR performance.[13] They also found that increasing the Mn/Co ratio above 1/2 led to decreased ORR catalytic activity. This is because the size was further increased with higher Mn/Co ratios (10−20 nm for $CoMn_2O_4$). Note that spinel $MnCo_2O_4$ crystallizes in a cubic structure, while $CoMn_2O_4$ crystallizes in a tetragonal structure in which Mn and Co cations occupy different sites. These graphene/metal−oxide hybrid composites exhibit comparable or even higher current density relative to the Pt counterpart, but the onset and half-wave potentials are still lower. Thus, it remains challenging to develop non-noble metal ORR catalysts with both currents and potentials comparable to or even surpassing that of Pt.

It is reported that the activities of nanoparticulated catalysts rely on the composition, shape, size, and structure.[25−28] According to Shao-Horn's design principle, the activity of oxides can be enhanced by tuning surface electronic structure such as transition-metal e_g-filling value and metal−oxygen covalency.[11] Oxides containing mixed transition-metal elements are favorable ORR catalysts as the variable metal valences enable electron hopping with the provision of surface redox centers to bind and activate molecular oxygen.[14,29] Moreover, downsizing metal oxide nanoparticles could be beneficial due to increased surface-atom exposure that contributes to not only catalytic sites but also surface metallicity.[30,31] As an estimation, the surface to total atom ratio of 2 nm oxide particle exceeds 25% (Supporting Information, Figure S1).

Received: March 6, 2015
Published: May 19, 2015

DOI: 10.1021/acs.inorgchem.5b00518
Inorg. Chem. 2015, 54, 5467−5474

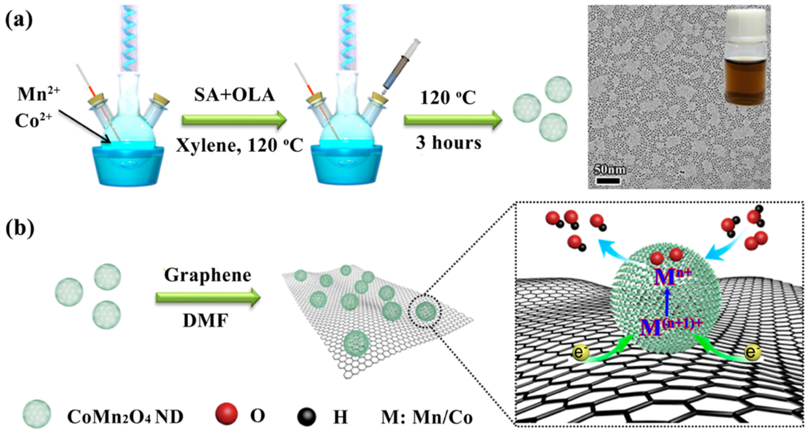

Figure 1. (a) Schematic synthesis of monodispersed $CoMn_2O_4$ NDs. The upper right shows the typical TEM image with the inset of the photo for the obtained colloid. (b) Schematic diagram of ORR on graphene-supported $CoMn_2O_4$ NDs.

Considering all these factors, it is desirable to develop metal−oxide nanoparticles with the combination of ultrasmall size (<3 nm) and multiple-valence composition for ORR/OER electrocatalysts. Herein, we report for the first time the preparation of ultrasmall (1.7−3 nm) and monodispersed $CoMn_2O_4$ NDs with tetragonal spinel phase using a facile and low-temperature reaction (120 °C) in xylene. Loaded on graphene support, the as-prepared mondispersed $CoMn_2O_4$ NDs are cheap yet highly efficient ORR/OER catalysts. This should shed light on the synthesis of monodispersed $CoMn_2O_4$ nanodots (NDs) as well as on their application as highly efficient electrocatalysts for ORR/OER, which are key reactions in fuel cells and rechargeable metal−air batteries.

■ EXPERIMENTAL SECTION

Chemicals and Materials. Manganese(II) acetate, cobalt dichloride, xylene, oleylamine, stearic acid, hexane, dimethylformamide, ethanol, graphite, and Nafion (5%) were purchased from Sigma-Aldrich. Concentrated nitric, hydrochloric, and sulfuric acid, potassium permanganate, and hydrogen peroxide (30%) were provided by Tianjin Guangfu Fine Chemical Research Institute. Carbon-supported Pt nanoparticles (Pt/C, 10 wt % Pt) was supplied by Johnson Matthey.

Reduced Graphene Oxide Synthesis. Graphite oxide (GO) was synthesized according to the modified Staudenmaier method.[32] Graphite (2.5 g), concentrated sulfuric acid (90 mL), concentrated nitric acid (30 mL), and potassium permanganate (12.5 g) were added to a 1000 mL three-necked round-bottom flask. The resulting solution was stirred for 2 h in an ice bath (0 to ca. −5 °C). Then, the solution was kept at 20 °C and stirred for 120 h. On completion of the reaction, the mixture was added slowly to 500 mL of water and stirred for 2 h. Subsequently, 15 mL of hydrogen peroxide was added, and the resulting precipitates were filtrated, washed with a 3% solution of HCl, and then repeatedly washed with water until the pH of the filtrate was 6. The GO precipitate was freeze-dried for 48 h under vacuum. The reduced graphene oxide (rGO) was prepared by thermal treatment of GO at 1000 °C in a cylindrical electric furnace under a flow of Ar gas for 30 min.

Synthesis of $CoMn_2O_4$ Nanodots. $CoMn_2O_4$ nanoparticles were synthesized according to a combined procedure with hot-injection method[33] and "heating up" route.[34,35] A solution of 15 mL of xylene, 2.670 g of oleylamine, 0.570 g of stearic acid, 0.115 g of manganese(II) acetate, and 0.043 g of cobalt dichloride in a three-necked flask was heated to 120 °C in air under magnetic stirring and was kept at this temperature for 30 min. Then, 1 mL of deionized water was injected into the solution under a vigorous stirring. The resulting solution was aged at 120 °C for 3 h. A total of 90 mL of ethanol was added to precipitate the nanocrystals, which was followed by centrifugation to retrieve the nanocrystals in powdery form. The as-synthesized NDs were well-dispersible in hexane. Bulk and 10 nm $CoMn_2O_4$ NDs were prepared as in our other report.[36]

The $CoMn_2O_4$ NDs were assembled on rGO surface as follows: 7 mg of $CoMn_2O_4$ NDs dispersed in 15 mL of hexane was added into 20 mL of dimethylformamide (DMF) solution of graphene (0.5 mg/mL), and the mixture was sonicated for 1 h. Ethanol (8 mL) was added after sonication, and the suspension was centrifuged at 9500 rpm for 10 min to obtain the $CoMn_2O_4$/rGO sample. $CoMn_2O_4$/rGO nanocomposites were annealed in air at 170 °C for 12 h to remove the surfactant.

Instrumentation. X-ray diffraction (XRD) patterns were recorded on a Rigaku Mini Flex 600 powder diffractometer (XRD, Rigaku Mini Flex 600 X-ray generator, Cu Kα radiation, $\lambda = 1.5406$ Å) at a scanning rate of 1° min^{-1} from 10 to 80°. Transmission electron microscopy (TEM) and high-resolution TEM specimens were prepared by depositing a drop of diluted NDs dispersion in hexane on copper grids coated with amorphous carbon. TEM imaging was obtained on Philips Tecnai F20 system operated at 200 kV with an energy-dispersive X-ray spectrometer (EDS). Nitrogen adsorption−desorption events were performed on a BEL-Mini adsorption analyzer. Raman spectra were collected using a confocal Raman microscope (DXR, Thermo-Fisher Scientific) with a 532 nm source from an argon ion laser. Elemental analysis was measured by inductively coupled plasma-atomic emission spectroscopy (ICP-9000, Thermo Jarrell-Ash Corp). Electrochemical measurements were performed with a computer-controlled workstation bipotentiostats (AFCBP1, Pine Instrument). A three-electrode system consisting of a rotation disk electrode (RDE), working electrode (5.61 mm in diameter), a saturated calomel electrode (SCE), and a platinum wire counter electrode was used.

Catalyst Preparation. The as-prepared $CoMn_2O_4$/rGO (5 mg) was suspended in a mixture of deionized water, ethanol, and Nafion (v/v/v = 4/1/0.7, 400 μL, 100 μL, 70 μL) to form a catalyst ink for electrochemistry measurements. Catalyst ink (9.0 μL) was deposited on the RDE working electrode and dried at ambient condition. Catalyst loading was ~0.319 mg cm^{-2} on the RDE. For comparison, electrocatalytic activity of the benchmark Pt/C was also investigated under the same condition.

Electrochemical Measurements. Polarization curves of ORR were obtained by linear sweep voltammetry scanning from 0.1 to −0.8 V versus SCE at a scan rate of 5 mV/s in O_2-saturated 0.1 M KOH with different rotating rates (400−2025 rpm). Polarization curves of oxygen evolution reaction were obtained by linear sweep voltammetry scanning from 0.1 to 0.85 V versus SCE at a scan rate of 5 mV/s in O_2-saturated 0.1 M KOH with RDE. Electrochemical impedance spectra were measured over a frequency range from 100 kHz to 100 mHz at a direct-current bias potential of 0.83 V at room temperature. Mott−Schottky plots were performed using PARSTAT 4000. Capacity measurements were conducted with 100 Hz frequency, in potential ranging from −1.2 to −0.5 V versus SCE. Chronoamperometry was collected to evaluate the catalyst durability at −0.3 V versus SCE with

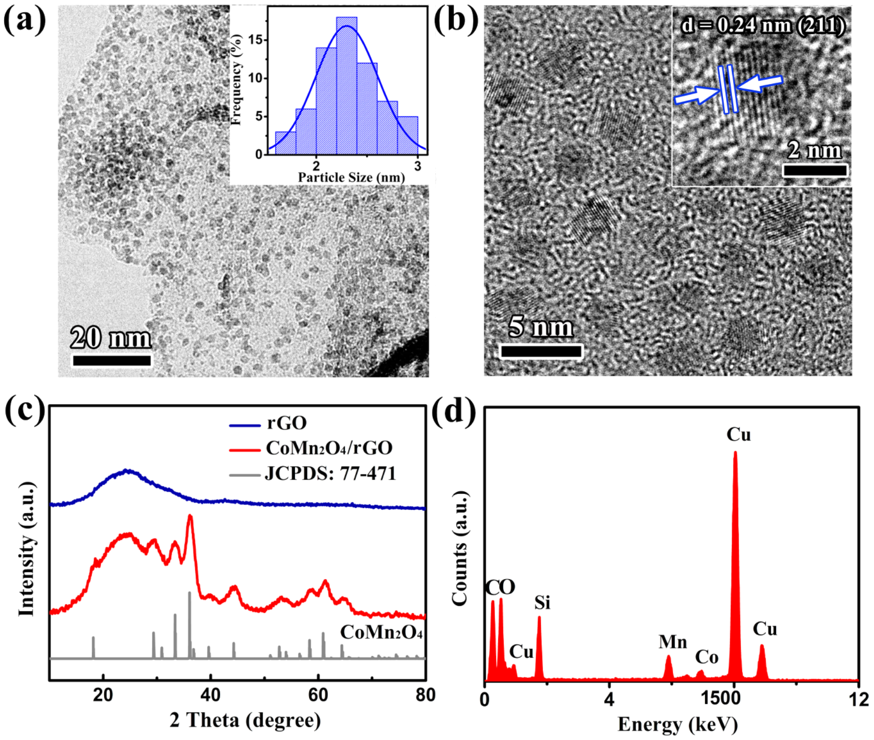

Figure 2. (a) TEM image of $CoMn_2O_4$/rGO. (inset) Particle size distribution histogram. (b) High-resolution TEM image of $CoMn_2O_4$ NDs. (c) XRD patterns of rGO, $CoMn_2O_4$/rGO, and standard $CoMn_2O_4$. (d) EDS spectrum of $CoMn_2O_4$/rGO.

the electrode rotating rate of 400 rpm in O_2-saturated 0.1 M KOH solution.

Reversible Hydrogen Electrode Calibration. In all measurements, an SCE was used as the reference electrode. It was calibrated against and converted to the reversible hydrogen electrode (RHE). The calibration was measured in the high-purity H_2 saturated 0.1 M KOH with a Pt wire as the working electrode. Cyclic voltammetry (CV) was performed at a scan rate of 1 mV s^{-1}, and the average of the two potentials at which the current crossed zero was taken to be the thermodynamic potential for the hydrogen electrode reaction (Supporting Information, Figure S2). In 0.1 M KOH solution, E(RHE) = E(SCE) + 0.991 V.

Calculation Method. The values of turnover frequency (TOF) were calculated by assuming that the surface metal atom is involved in the catalysis. The TOF values are obtained by the following equation:

$$\mathrm{TOF} = \frac{i_k \times S}{4 \times e \times N_s} \tag{1}$$

where i_k (mA cm^{-2}) is the kinetic current density at 0.85 V, S (0.247 cm^2) is the area of electrode, e (1.602×10^{-19} C) is the electron charge, the number four means four electrons per mole of O_2, and N_s is the number of active surface atoms (here we assume only Mn/Co atoms are active). The surface to total atom ratio of oxide particle is ~25% (Supporting Information, Figure S1).

■ RESULTS AND DISSCUSSION

Figure 1a illustrates the preparation of monodispersed $CoMn_2O_4$ NDs. Inspired from the classic hot-injection[33] and heating up route[34,35] to prepare monodispersed NDs, the present synthetic strategy combines two processes that include the injection of water into the hot solution containing Mn/Co precursors, and the formation and growth of nanocrystalline oxides upon heating. This method has been used to prepare manganese oxide nanocrystals with various shapes[37] in which oleyamine is not only a surfactant but also a base to increase the pH of the reaction solution and consequently influences the nucleation process. The manganese acetate and cobalt chloride first reacted with water and generated manganese hydroxide and cobalt hydroxide in the presence of oleylamine.[37] Then, $CoMn_2O_4$ NDs were obtained from decomposition of hydroxide, which mainly contributes to the nucleation. Stearic acid (SA) was used as the cosurfactant along with oleylamine (OLA), preventing agglomeration of the generated nanocrystals. It is reported that other carboxylic acid (e.g., oleic acid) was used as cosurfactant; the size of nanocrystal oxides was more than 6.2 nm.[37] Thus, we used SA as the cosurfactant to prepare ultrasmall $CoMn_2O_4$ NDs (below 3 nm). This synthesis can be readily scaled up since it involves only inexpensive, nontoxic reagents and proceeds at mild condition (120 °C in air), without the need of organometallic compounds and inert atmospheres. Additionally, the synthetic method was simple and reproducible as verified by TEM (Supporting Information, Figure S3). The monodispersed nanoparticles are ultrasmall (below 3 nm) and well-dispersible in organic solvents (e.g., hexane and DMF) to form a homogeneous colloid solution. Moreover, as schematically illustrated in Figure 1b, $CoMn_2O_4$ NDs can be uniformly distributed on electrically conductive substrates such as graphene. This simultaneously affords abundant surface redox sites and facile electron transfer path for ORR electrocatalysis. A direct self-assembly method was used to deposit monodispersed $CoMn_2O_4$ NDs on rGO sheet (see the Experimental Section for details and Supporting Information, Figure S4) as reported previously.[38] Mixing two immiscible solutions ($CoMn_2O_4$ in hexane and rGO in DMF) via sonication was an essential step to maintain the desired size and morphology of oxides. The graphene transferred to the upper hexane solution (Figure S4b) and $CoMn_2O_4$ NDs would be adsorbed on the surface of graphene. For comparison, pure hexane was added into DMF solution of graphene, and the obtained mixture was sonicated for 1 h. The graphene still dispersed in DMF solution (Figure S4c). Therefore, $CoMn_2O_4$ NDs can be assembled on the graphene surface tightly, which may be due to the absorption effect of functional groups on graphene. The ethanol was added to form a homogeneous solution (Figure S4d), and then $CoMn_2O_4$/rGO nanocomposites can be obtained by centrifugation.

Figure 2a shows the typical TEM image of the synthesized $CoMn_2O_4$ NDs supported on reduced graphene oxide ($CoMn_2O_4$/rGO) after heating treatment. Clearly, $CoMn_2O_4$ NDs were dispersed on rGO sheet, with relatively narrow size distribution between 1.7 and 3 nm. From high-resolution TEM imaging (Figure 2b), the observed lattice fringe was consistent with the neighboring distance of $CoMn_2O_4$ (211) planes. Powder X-ray diffraction (XRD) revealed the nanocrystalline nature of the obtained sample (Figure 2c). Despite severe peak broadening due to ultrasmall crystallite size, the reflections could be readily indexed to the tetragonal spinel phase of $CoMn_2O_4$ (JCPDS Card No. 77−471). Energy-dispersive spectroscopy (EDS) analysis indicated that the Mn/Co ratio was ~2 in the oxide (Figure 2d).

In addition, both Co/Mn−O vibrations and D/G bands could be detected in the Raman spectra (Figure 3), suggesting the copresence of spinel-type metal oxide and rGO. The mass loading amount of $CoMn_2O_4$ in $CoMn_2O_4$/rGO was ~30% analyzed by inductive coupled plasma-atomic emission spectrometer (ICP-AES). Furthermore, nitrogen adsorption/desorption isotherms (at 77 K) of $CoMn_2O_4$/rGO were measured (Figure 4). The isotherm displays a typical IUPAC type-IV adsorption/desorption behavior, suggesting mesoporous structure. The determined Brunauer−Emmett−Teller (BET) specific surface area of $CoMn_2O_4$/rGO nanocomposite is 412 $m^2\ g^{-1}$. The corresponding pore size distribution (PSD) of mesopores is centered at 3.7 nm, according to the Barrett−Joyner−Halenda (BJH) method.

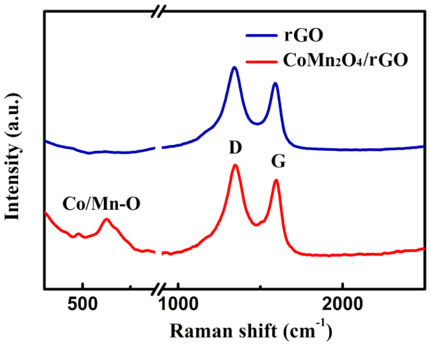

Figure 3. Raman spectra of rGO and $CoMn_2O_4$/rGO.

X-ray photoelectron spectroscopy (XPS) was employed to investigate the surface chemical state of the synthesized $CoMn_2O_4$/rGO. The Mn 2p spectra (Figure 5a) could be fitted with two pairs of spin−orbit doublets deconvoluted peaks, which are indicative of Mn^{2+} and Mn^{3+} oxidation states.[39] The sum peak position of Mn $2p_{3/2}$ was located at 641.8 eV. Similarly, the Co 2p spectra (Figure 5b) consisted of two pairs of spin−orbit doublets and four shakeup satellites, revealing the coexistence of Co^{2+} and Co^{3+}.[39] From Gaussian fitting of the peak areas, the Mn(II)/Mn(III) and Co(II)/Co(III) atomic ratios were 0.13 and 3.81, respectively. These results indicate the presence of multiple valence on the oxide surface with dominant Mn^{3+} and Co^{2+}. Additionally, the C 1s spectrum of $CoMn_2O_4$/rGO showed the presence of abundant oxygen functional groups (Figure 6), which were proposed to increase the interfacial interaction between graphene and metal oxide through a C−O−metal bridge.[40]

The synthesized $CoMn_2O_4$/rGO was afforded on a rotating glass carbon electrode to investigate the ORR electrocatalytic activity in 0.1 M KOH solution. In comparison, the other four samples of rGO, $CoMn_2O_4$ NDs supported on Vulcan XC-72 carbon ($CoMn_2O_4$/VC, Figure 7), 10 nm $CoMn_2O_4$ nanoparticles (NPs) supported on rGO (10 nm $CoMn_2O_4$/rGO), and commercial Pt/C (10 wt % Pt) were also tested.

Meanwhile, we also studied the mass loading amount of 20 and 40 wt % ultrasmall $CoMn_2O_4$ in the composites. Supporting Information, Figure S5a shows the Raman spectra for three different loading amounts of $CoMn_2O_4$. The peak intensity of Co/Mn−O was decreased in the composites as the mass loading amount of oxides decreased. Furthermore, the electrochemical measurement showed that content of 30 wt % $CoMn_2O_4$ was found to obtain the best performance (Supporting Information, Figure S5b). This is due to a balance of particle density, surface area, and electron conductivity in the composites. Thus, the ORR activities of 30 wt % $CoMn_2O_4$ sample were detailedly evaluated in our studies. Figure 8a shows the typical linear sweeping voltammograms of different catalysts at the potential scanning rate of 5 mV s^{-1} and the rotating rate of 400 revolutions per minute (rpm). The cathodic current in O_2-saturated electrolyte could be attributed mainly to the electrocatalytic ORR, as viewed from the negligible current response recorded at Ar atmosphere. The capacitive currents were measured and deducted (see Supporting Information, Figure S6). The rGO substrate itself was electrochemically active but showed only low ORR current and potential. Surprisingly, the $CoMn_2O_4$/rGO nanocomposite exhibited superior catalytic activity to the benchmark Pt/C. The onset potential of $CoMn_2O_4$/rGO was ~0.95 V, which was similar to previously reported $MnCo_2O_4$/N-rmGO in 1 M

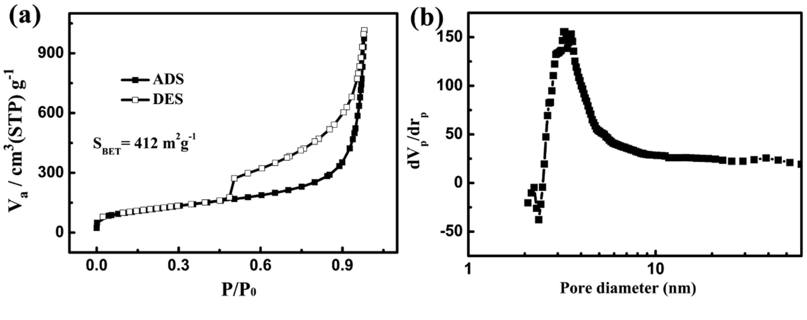

Figure 4. (a) Nitrogen adsorption/desorption isotherms (at 77 K) of $CoMn_2O_4$/rGO, (b) pore size distribution determined from the BJH method.

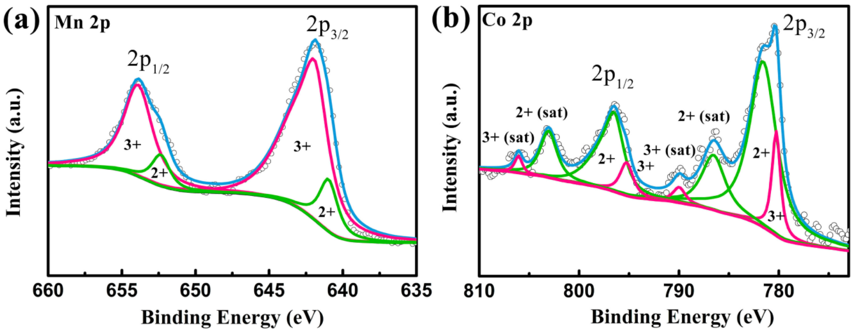

Figure 5. (a) Mn 2p and (b) Co 2p XPS spectra of the synthesized $CoMn_2O_4$/rGO.

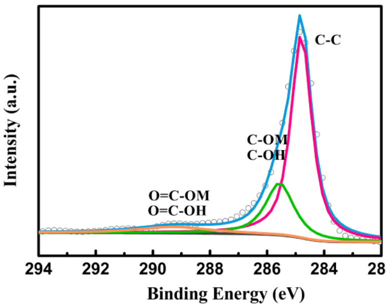

Figure 6. High-resolution XPS spectra of C 1s core levels in the $CoMn_2O_4$/rGO hybrid.

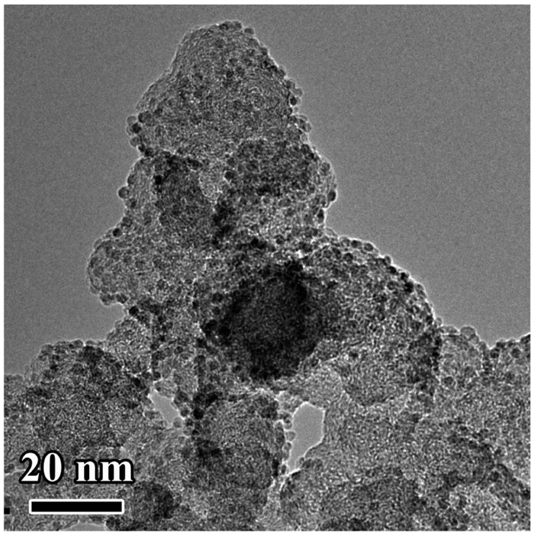

Figure 7. TEM image of $CoMn_2O_4$ NDs supported on Vulcan XC-72 carbon.

KOH and 30 mV higher in 0.1 M KOH.[13] It is reported that in 1 M KOH, the ORR onset potential was more positive and that the current density was smaller than that in 0.1 M KOH. This is due to facilitated oxygen activation, low bulk concentration, and diffusion coefficient of O_2 in 1 M KOH electrolyte.[41] The half-wave potential of $CoMn_2O_4$/rGO was 0.89 V, which was 20 mV higher than that of Pt/C and was among the best results reported for nonprecious catalysts (Supporting Information, Table S1).[42] Compared to $CoMn_2O_4$/VC, $CoMn_2O_4$/rGO delivered a ~50 mV lower overpotential, implying that graphene played an important role in enhancing the ORR performance. Furthermore, the ultrasmall $CoMn_2O_4$/rGO outperformed 10 nm $CoMn_2O_4$/rGO and bulk $CoMn_2O_4$ (Supporting Information, Figure S7), in terms of higher onset potential and limiting current density (based on the geometric area of the electrode). The mass activities (0.85 V) were calculated to be 254.7, 16.5, and 3.34 A g^{-1}_{metal} for 2.3 nm $CoMn_2O_4$/rGO, 10 nm $CoMn_2O_4$/rGO, and bulk $CoMn_2O_4$, respectively. This is apparently attributed to the smaller particle size for providing more active surface atoms.

To understand the unprecedented catalytic ability of the hybrid $CoMn_2O_4$/rGO, we performed Mott−Schottky analysis and electrochemical impedance spectroscopy (EIS) measurements. Figure 8b displays the Mott−Schottky profiles of rGO, $CoMn_2O_4$/rGO, and $CoMn_2O_4$/VC. The plots showed a positive slope, suggesting typical n-type semiconducting behavior.[43,44] The charge carrier concentration (N_D) can be determined from the slope of the curves (see Supporting Information).[43,44] The calculated N_D of $CoMn_2O_4$/rGO (1.18×10^{24} cm^{-3}) was one magnitude that of $CoMn_2O_4$/VC (1.08×10^{23} cm^{-3}) and nearly five magnitudes that of reported MnO_2 (Supporting Information, Figure S8).[45] This result clearly suggests positive attribution of rGO, multiple-valence metals, and ultrasmall oxide particles to the charge transporting ability, which largely dictates the rate-determining step of ORR mediated by redox sites of transition-metal oxides.[1,5,11] In the EIS Nyquist plots (Supporting Information, Figure S9) measured at 0.83 V, $CoMn_2O_4$/rGO showed a smaller compressed semicircle than that of $CoMn_2O_4$/VC, indicating a lower charge transfer resistance of the former. The smaller charge transfer resistance was possibly due to the intimate interaction between the rGO substrate and the $CoMn_2O_4$ NDs, which enhanced electron transfer in electrocatalytic ORR process.

The ORR kinetics was also evaluated from a set of voltammetry profiles collected on rotational electrodes (Supporting Information, Figure S10). The currents at different rotating speeds were used to construct the Koutecky−Levich (K−L) plots, where the electron number transferred per O_2 molecule (n) and kinetic current (i_k) could be determined from the slope and intercept of the fitted linear line, respectively.[46,47] Both plots (Supporting Information, Figure S11) of $CoMn_2O_4$/rGO and Pt/C showed similar slopes and n value close to 4, demonstrating favorable four-electron ORR pathway. The calculated i_k data were applied to construct the Tafel plots (Figure 8c). Having similar Tafel slops, the superior activity of $CoMn_2O_4$/rGO over Pt/C was further verified from the higher kinetic current at a given potential. The kinetic current of $CoMn_2O_4$/rGO at 0.90 V was measured to be 3.22 mA/cm^2, twice that of Pt/C (1.61 mA/cm^2). The specific activity and mass activity obtained from the kinetic current attained 3.93 A m^{-2} and 254.7 A g^{-1}_{metal} for $CoMn_2O_4$/rGO, again surpassing

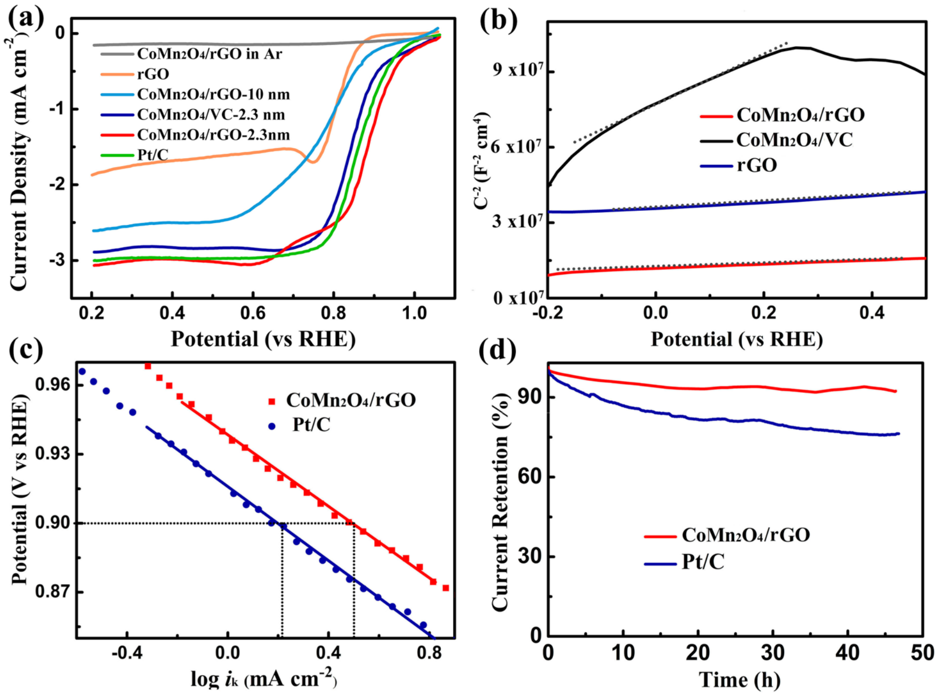

Figure 8. (a) Polarization curves of 10 nm and ultrasmall $CoMn_2O_4$/rGO, rGO, $MnCo_2O_4$/VC, and Pt/C in O_2-saturated and Ar-saturated 0.1 M KOH at a potential sweep rate of 5 mV/s and at 400 rpm. The capacitive currents were corrected for polarization curves. (b) Mott–Schottky plots of $CoMn_2O_4$/rGO, rGO, and $CoMn_2O_4$/VC. (c) Tafel plots of $CoMn_2O_4$/rGO and Pt/C derived from the ORR voltammogram. (d) Chronoamperometric profiles of $CoMn_2O_4$/rGO and Pt/C at 0.7 V in O_2-saturated 0.1 M KOH.

that of Pt/C. Furthermore, the TOF calculated according to the relation[46] was 0.1 atom^{-1} s^{-1} at 0.85 V for $CoMn_2O_4$/rGO, comparable to that of the benchmark Pt/C.

In addition to remarkable activity, the synthesized $CoMn_2O_4$/rGO exhibited respectable catalytic durability, as shown in Figure 8d. At a constant potential of 0.7 V, the ORR current density generated by $CoMn_2O_4$/rGO sustained more than 92% over 46 h of continuous polarization, while the benchmark Pt/C showed a quick current decay of 24%. Notably, the good dispersibility and ultrasmall particle size of $CoMn_2O_4$ in the composite were well-retained after the extended durability test, as demonstrated by TEM image (Figure 2a and Figure 9). In comparison, there were severe particle detaching and agglomeration for the Pt/C catalyst (Supporting Information, Figure S12). The superior electrocatalytic stability of $CoMn_2O_4$/rGO could be partially ascribed to the porous rGO support that firmly anchored the $CoMn_2O_4$ NDs with a uniform distribution.

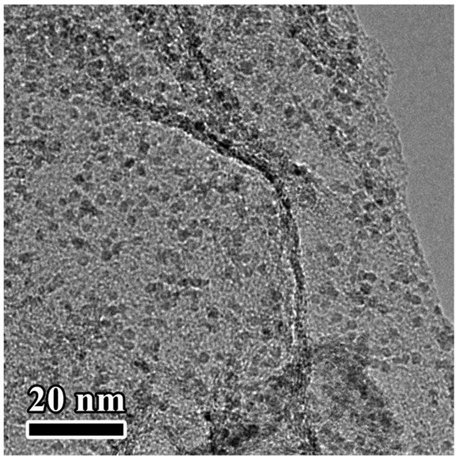

Figure 9. TEM image of $CoMn_2O_4$/rGO after long-term durability test.

Lastly, it deserves to be mentioned that the obtained $CoMn_2O_4$/rGO is also active for electrocatalysis of the oxygen evolution reaction (OER). In alkaline electrolyte, $CoMn_2O_4$/rGO gave a considerable low OER onset potential of 1.49 V and afforded a current density of 10 mA cm^{-2} at a low potential of 1.54 V (Figure 10a). The polarization curves were corrected for solution resistance, which was performed to be ca. 35 Ω by electrochemical impedance spectrum. Figure 10b shows the Tafel plots of the catalysts. The Tafel slope of $CoMn_2O_4$/rGO is 56 mV dec^{-1}, which is much smaller than that of rGO (156 mV dec^{-1}) and Pt/C (280 mV dec^{-1}), indicating high OER activity for $CoMn_2O_4$/rGO. As previously proposed, the OER potential at the current density of 10 mA cm^{-2} is a figure of merit related to solar fuel synthesis.[48] Here we choose the potential separation between ORR (at the current of 1 mA cm^{-2}) and OER (at 10 mA cm^{-2}) as a metric to evaluate the performance of bifunctional oxygen electrocatalysts. The value was ∼0.65 V for $CoMn_2O_4$/rGO, which is lower than that of recently reported representative oxygen electrodes such as Co_xO_y/N-doped carbon (0.86 V)[48] and CoO/N-doped graphene (0.76 V).[49] This result indicates that $CoMn_2O_4$/rGO is among the most active bifunctional ORR/OER catalysts reported to date.[12,17,49,50] The exciting catalytic performance of $CoMn_2O_4$/rGO can be attributed to several factors. First, the $CoMn_2O_4$ surface occurs with Mn(II)/Mn(III) and Co(II)/Co(III) multivalent states that mediate the redox reaction concurrent with the oxygen reduction. XPS analysis reveals dominantly enriched surface Mn(III), which has been proposed as active species for oxygen electrocatalysis.[12,42,51] Second, the ultrasmall size (typically 2.3 nm) of $CoMn_2O_4$ dots exposes

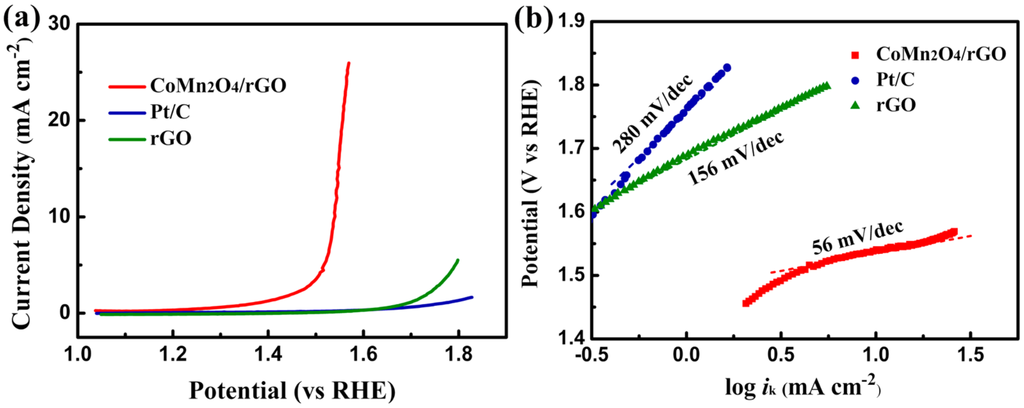

Figure 10. (a) Oxygen evolution currents of $CoMn_2O_4$/rGO, rGO, and Pt/C electrodes in 0.1 M KOH electrolyte at a potential scan rate of 10 mV/s. (b) Tafel plots of $CoMn_2O_4$/rGO, rGO, and Pt/C.

significantly high proportion of surface atoms to bind and activate oxygen molecules. Third, the rGO substrate strongly coupling metal oxide favors high concentration of charge carrier and facile electron conduction (Figure 8b). Additional benefits include porous structure, high specific surface area, and high particle dispersion, which is advantageous for heterogeneous catalysis.

■ CONCLUSION

In conclusion, we developed a facile route to synthesize $CoMn_2O_4$ NDs (below 3 nm) that are monodispersed on graphene using low-cost raw materials at mild temperature of 120 °C and ambient atmosphere. We demonstrated that the composite of graphene-supported $CoMn_2O_4$ NDs was highly active toward ORR in alkaline solution, exhibiting a ~20 mV more positive half-wave potential, a higher kinetic current density, and a much better catalytic durability compared to Pt/C. Furthermore, $CoMn_2O_4$/rGO exhibited exceptional OER activity with a low potential of 1.54 V at the current density of 10 mA cm^{-2} and a small Tafel slope of 56 mV/dec. Therefore, the composite of graphene-supported $CoMn_2O_4$ NDs showed a promising bifunctional electrocatalytic ORR/OER with considerably low overpotential due to the strong carbon−metal oxide interaction. This study indicates great potential to attain Pt-like electrocatalytic activity for nonprecious 3d metal oxides by downsizing into NDs (below 3 nm) and anchoring oxide colloids on graphene-based support.

■ ASSOCIATED CONTENT

Ⓢ Supporting Information

Crystal structure, cyclic voltammograms, TEM images, photos, Raman spectra, polarization curves, Mott−Schottky plots, electrochemical impedance spectra, and Koutecky−Levich (K−L) plots. The Supporting Information is available free of charge on the ACS Publications website at DOI: 10.1021/acs.inorgchem.5b00518.

■ AUTHOR INFORMATION

Corresponding Author

*Phone/Fax: +86-22-23506808. E-mail: chenabc@nankai.edu.cn.

Notes

The authors declare no competing financial interest.

■ ACKNOWLEDGMENTS

This work was supported by the National Programs of 973 (2011CB935900), NSFC (21231005 and 21322101), and MOE (B12015 and ACET-13-0296).

■ REFERENCES

(1) Kinoshita, K. *Electrochemical Oxygen Technology*; Wiley: New York, 1992.

(2) Desmond Ng, J. W.; Gorlin, Y.; Hatsukade, T.; Jaramillo, T. F. *Adv. Energy Mater.* **2013**, *3*, 1545.

(3) Bing, Y. H.; Liu, H. S.; Zhang, L.; Ghosh, D.; Zhang, J. J. *Chem. Soc. Rev.* **2010**, *39*, 2184.

(4) Cao, R.; Lee, J. S.; Liu, M.; Cho, J. *Adv. Energy Mater.* **2012**, *2*, 816.

(5) Black, R.; Oh, S. H.; Lee, J. H.; Yim, T.; Adams, B.; Nazar, L. F. *J. Am. Chem. Soc.* **2012**, *134*, 2902.

(6) Cheng, F.; Chen, J. *Chem. Soc. Rev.* **2012**, *41*, 2172.

(7) Chen, C.; Kang, Y.; Huo, Z.; Zhu, Z.; Huang, W.; Xin, H.; Snyder, J. D.; Li, D.; Herron, J. A.; Mavrikakis, M.; Chi, M.; More, K. L.; Li, Y.; Markovic, N. M.; Somorjai, G. A.; Yang, P.; Stamenkovic, V. R. *Science* **2014**, *342*, 1339.

(8) Alia, S. M.; Pylypenko, S.; Neyerlin, K. C.; Cullen, D. A.; Kocha, S. S.; Pivovar, B. S. *ACS Catal.* **2014**, *4*, 2680.

(9) Wu, J.; Yang, H. *Acc. Chem. Res.* **2013**, *46*, 1848.

(10) Chen, S.; Wei, Z.; Qi, X.; Dong, L.; Guo, Y.; Wan, L.; Shao, Z.; Li, L. *J. Am. Chem. Soc.* **2012**, *134*, 13252.

(11) Suntivich, J.; Gasteiger, H. A.; Yabuuchi, N.; Nakanishi, H.; Goodenough, J. B.; Shao-Horn, Y. *Nat. Chem.* **2011**, *3*, 546.

(12) Gorlin, Y.; Lassalle-Kaiser, B.; Benck, J. D.; Gul, S.; Webb, S. M.; Yachandra, V. K.; Yano, J.; Jaramillo, T. F. *J. Am. Chem. Soc.* **2013**, *135*, 8525.

(13) Liang, Y.; Wang, H.; Zhou, J.; Li, Y.; Wang, J.; Regier, T.; Dai, H. *J. Am. Chem. Soc.* **2012**, *134*, 3517.

(14) Zhu, H.; Zhang, S.; Huang, Y.; Wu, L.; Sun, S. *Nano Lett.* **2013**, *13*, 2947.

(15) Cao, B. F.; Neuefeind, J. C.; Adzic, R. R.; Khalifah, P. G. *Inorg. Chem.* **2015**, *54*, 2128.

(16) Zaharieva, I.; Najafpour, M. M.; Wiechen, M.; Haumann, M.; Kurz, P.; Dau, H. *Energy Environ. Sci.* **2011**, *4*, 2400.

(17) Ma, T.; Dai, S.; Jaroniec, M.; Qiao, S. *J. Am. Chem. Soc.* **2014**, *136*, 13925.

(18) Hardin, W. G.; Slanac, D. A.; Wang, X. Q.; Dai, S.; Johnston, K. P.; Stevenson, K. J. *J. Phys. Chem. Lett.* **2013**, *4*, 1254.

(19) El-Deab, M. S.; Ohsaka, T. *Angew. Chem., Int. Ed.* **2006**, *45*, 5963.

(20) Zhang, K.; Han, X. P.; Hu, Z.; Zhang, X. L.; Tao, Z. L.; Chen, J. *Chem. Soc. Rev.* **2015**, *44*, 699.

(21) Kim, J.; Yin, X.; Tsao, K. C.; Fang, S.; Yang, H. *J. Am. Chem. Soc.* **2014**, *136*, 14646.

(22) Cheng, F. Y.; Shen, J.; Peng, B.; Pan, Y. D.; Tao, Z. L.; Chen, J. *Nat. Chem.* **2011**, *3*, 79.
(23) Liang, Y.; Li, Y.; Wang, H.; Zhou, J.; Wang, J.; Regier, T.; Dai, H. *Nat. Mater.* **2011**, *10*, 780.
(24) Guo, S.; Zhang, S.; Wu, L.; Sun, S. *Angew. Chem., Int. Ed.* **2012**, *51*, 11770.
(25) Proch, S.; Wirth, M.; White, H. S.; Anderson, S. L. *J. Am. Chem. Soc.* **2013**, *135*, 3073.
(26) Xia, Y.; Yang, H.; Campbell, C. T. *Acc. Chem. Res.* **2013**, *46*, 1671.
(27) Guo, S.; Zhang, S.; Sun, S. *Angew. Chem., Int. Ed.* **2013**, *52*, 8256.
(28) Meng, Y.; Song, W.; Huang, H.; Ren, Z.; Chen, S. Y.; Suib, S. L. *J. Am. Chem. Soc.* **2014**, *136*, 11452.
(29) Rios, E.; Gautier, J. L.; Poillerat, G.; Chartier, P. *Electrochim. Acta* **1998**, *44*, 1491.
(30) Tompsett, D. A.; Islam, M. S. *J. Phys. Chem. C* **2014**, *118*, 25009.
(31) Tompsett, D. A.; Parker, S. C.; Islam, M. S. *J. Am. Chem. Soc.* **2014**, *136*, 1418.
(32) McAllister, M. J.; Li, J. L.; Adamson, D. H.; Schniepp, H. C.; Abdala, A. A.; Liu, J.; Herrera-Alonso, M.; Milius, D. L.; Car, R. P.; Aksay, I. A. R. *Chem. Mater.* **2007**, *19*, 4396.
(33) Murray, C. M.; Norris, D. J.; Bawendi, M. G. *J. Am. Chem. Soc.* **1993**, *115*, 8706.
(34) Park, J.; An, K. J.; Hwang, Y.; Park, J. G.; Noh, H. J.; Kim, J. Y.; Park, J. H.; Hwang, N. M.; Hyeon, T. *Nat. Mater.* **2004**, *3*, 891.
(35) Kwon, S. G.; Piao, Y.; Park, J.; Angappane, S.; Jo, Y.; Hwang, N. M.; Park, J. G.; Hyeon, T. *J. Am. Chem. Soc.* **2007**, *129*, 12571.
(36) Du, J.; Zhang, T. R.; Cheng, F. Y.; Chu, W. S.; Wu, Z. Y.; Chen, J. *Inorg. Chem.* **2014**, *53*, 9106.
(37) Yu, T.; Moon, J.; Park, J.; Park, Y. I.; Na, H. B.; Kim, B. H.; Song, I. C.; Moon, W. K.; Hyeon, T. *Chem. Mater.* **2009**, *21*, 2272.
(38) Guo, S. J.; Sun, S. H. *J. Am. Chem. Soc.* **2012**, *134*, 2492.
(39) Yu, L.; Zhang, L.; Wu, H. B.; Zhang, G. Q.; Lou, X. W. *Energy Environ. Sci.* **2013**, *6*, 2664.
(40) Zhou, G.; Wang, D. W.; Yin, L. C.; Li, N.; Li, F.; Cheng, H. M. *ACS Nano* **2012**, *6*, 3214.
(41) Blizanac, B. B.; Ross, P. N.; Markovic, N. M. *Electrochim. Acta* **2007**, *52*, 2264.
(42) Risch, M.; Stoerzinger, K. A.; Maruyama, S.; Hong, W. T.; Takeuchi, I.; Shao-Horn, Y. *J. Am. Chem. Soc.* **2014**, *136*, 5229.
(43) Gao, E. P.; Wang, W. Z.; Shang, M.; Xu, J. H. *Phys. Chem. Chem. Phys.* **2011**, *13*, 2887.
(44) Das, J. N. *Z. Phys.* **1958**, *151*, 345.
(45) L'Hostis, V.; Dagbert, C.; Féron, D. *Electrochim. Acta* **2003**, *48*, 1451.
(46) Lima, F. H. B.; Calegaro, M. L.; Ticianelli, E. A. *J. Electroanal. Chem.* **2006**, *590*, 152.
(47) Paulus, U. A.; Wokaun, A.; Scherer, G. G. *J. Phys. Chem. B* **2002**, *106*, 4181.
(48) Masa, J.; Xia, W.; Sinev, I.; Zhao, A.; Sun, Z.; Grützke, S.; Weide, P.; Muhler, M.; Schuhmann, W. *Angew. Chem., Int. Ed.* **2014**, *53*, 8508.
(49) Mao, S.; Wen, Z.; Huang, T.; Hou, Y.; Chen, J. *Energy Environ. Sci.* **2014**, *7*, 609.
(50) Trotochaud, L.; Samantha, L.; Ranney, J. K.; Boettcher, S. W. *J. Am. Chem. Soc.* **2014**, *136*, 6744.
(51) Takashima, T.; Hashimoto, K.; Nakamura, R. *J. Am. Chem. Soc.* **2012**, *134*, 1519.